Matter

CellPress

Article

Strain- and Strain-Rate-Invariant Conductance in a Stretchable and Compressible 3D Conducting Polymer Foam

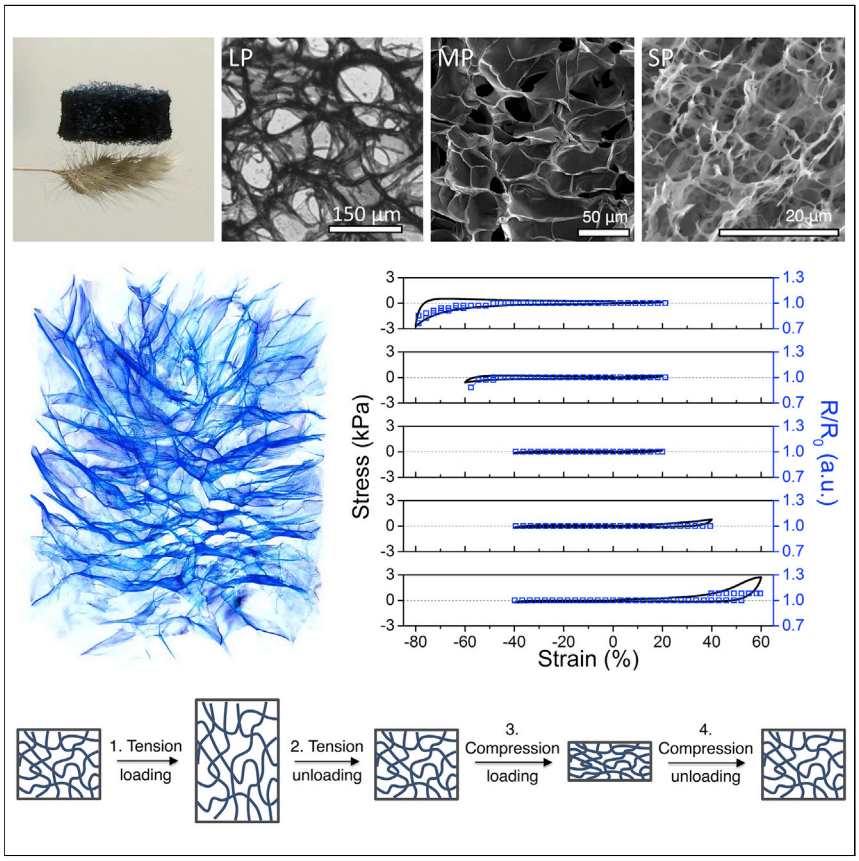

A stretchable conductor is a crucial component required as electrodes for signal probing or interconnects between various electrical components in stretchable electronics. Current approaches for stretchable conductors use strain engineering or composite materials. Here, we demonstrate a conducting polymer foam in which strain- and strain-rate-invariant conductance and compliance are synergistically engineered into a singular entity. The cellular nature of the materials also provides accommodation for both compressive and tensile strains while offering breathability, which opens up new possibilities for stretchable conductors.

3 Understanding
Dependency and conditional studies on material behavior

Gan Chen, Reza Rastak, Yue Wang, Hongping Yan, Vivian Feig, Yuxin Liu, Yuanwen Jiang, Shucheng Chen, Feifei Lian, Francisco Molina-Lopez, Lihua Jin, Kiara Cui, Jong Won Chung, Eric Pop, Christian Linder, Zhenan Bao

zbao@stanford.edu

HIGHLIGHTS

PEDOT aerogels with controlled pore size and Young's moduli between 10 and 300 kPa

Strain- and strain-rate-invariant conductance

Remarkable cycling stability under repeated tensile and compressive strain

Finite-element simulation using X-ray tomography reconstruction for stretching

Chen et al., Matter *1*, 205–218
July 10, 2019
https://doi.org/10.1016/j.matt.2019.03.011

Matter

CellPress

Article

Strain- and Strain-Rate-Invariant Conductance in a Stretchable and Compressible 3D Conducting Polymer Foam

Gan Chen,[1,9] Reza Rastak,[2,9] Yue Wang,[3,8,9] Hongping Yan,[4] Vivian Feig,[1] Yuxin Liu,[5] Yuanwen Jiang,[3] Shucheng Chen,[3] Feifei Lian,[6] Francisco Molina-Lopez,[3] Lihua Jin,[2,3] Kiara Cui,[3] Jong Won Chung,[3,7] Eric Pop,[6] Christian Linder,[2] and Zhenan Bao[3,10,*]

SUMMARY

Advances in stretchable conductors have been one of the main driving forces behind the realization of wearable and epidermal electronics. However, retaining constant strain-property relationships under varying strain and strain rate remains a challenge. Here, we demonstrate a 3D structuring approach toward strain-accommodating, biocompliant conductors. In contrast to previous stretchable conductors, this method leads to polymeric materials with conductance that has zero dependence on (1) both tensile and compressive strain over an 80% strain range, and (2) strain rate from 2.5%/min to 2,560%/min. Their Young's moduli can be controllably tuned between 10 and 300 kPa. In addition, these conductors are ultra-lightweight and can be molded into virtually any shape and size. Their properties mimic the dynamic and softness of biological systems, rendering this a versatile platform for designing electronic materials that can potentially form intimate interfaces with humans.

INTRODUCTION

Recent development in wearable and epidermal electronics that can form intimate interfaces with the biological systems under various dynamic conditions has opened a new dimension in personal healthcare and soft robotics.[1–6] Conductors that mimic the strain-property relationships of the human body, i.e., retaining electrical properties under stretching or compression, have been one of the key components that is advancing the field.[5,7] There are three general approaches to such conductors. The first approach is via strain engineering, where stiff materials such as metals are patterned into wavy ribbons that can extend in length under tension and used to connect various rigid electronic components.[8,9] Creating Kirigami cuts in a stiff film, such as carbon nanotube composite and graphene sheets, has also been demonstrated as a feasible approach to dissipate tensile strain.[10,11] Despite the high flexibility in material choices, such strain-engineering methods cause the structures to bend out of plane in the direction perpendicular to the stretching direction, which becomes challenging for device encapsulation or stacking multiple layers of electronic components to impart multi-functionality. The large difference between the intrinsic stiffness of these conductors and biological systems also limits the possibility of forming direct interfaces. The second approach is creating composites by combining an elastic matrix and a conductive filler, such as metal or carbon-based nanostructures.[12–16] A wide variety of materials can be used for both components, rendering this method highly versatile. However, the electrical properties of composites are percolation dependent. Strain causes changes in percolation pathways,

Progress and Potential

In contrast to previous efforts such as nanocomposites or intrinsically stretchable conductors, we demonstrated a 3D structuring approach for PEDOT:PSS that can lead to electrical resistance that is independent of strain and strain rate over a broad range, under both compression and tension and exhibiting remarkable cycling stability. Their Young's moduli can be controllably tuned between 10 and 300 kPa. Their properties mimic the dynamic and compliance of biological systems, rendering this a versatile platform for designing electronic materials that can potentially form intimate interfaces with humans.

which leads to conductivity change. Third, intrinsically stretchable conductors have been demonstrated via molecular engineering of conjugated polymers or by incorporating multi-functional additives.[17–20] These materials are solution processable, have significantly lower stiffness compared with the inorganic counterparts, and show high maximum tensile strain. However, they also exhibit strain-dependent electrical properties, typically non-reversible or with large hysteresis, due to changes at the molecular and supramolecular levels when elongated.

In this work, we demonstrate a 3D structuring approach for conjugated polymers where strain- and strain-rate-invariant conductance and compliance are synergistically engineered into a singular entity. The cellular nature of the materials also provides accommodation for both compressive and tensile strains that occur under different human motions while offering breathability, which is a desirable combination of features that has been hitherto difficult to impart in stretchable conductors.

RESULTS AND DISCUSSION

Strain-accommodating poly(3,4-ethylenedioxythiophene):polystyrene sulfonate (PEDOT:PSS) **1** 3D networks were synthesized in the presence of a plasticizing co-dopant, 4-(3-butyl-1-imidazolio)-1-butanesulfonic acid triflate (BIBSAT) **2**. This additive serves as an effective plasticizing co-dopant that simultaneously enhances the conductivity and maximum tensile strain of PEDOT:PSS by a significant amount.[17] It was also found to induce PEDOT aggregation due to the screening effect that changes the Coulombic interaction between the PEDOT and PSS. The mixture formed a gel upon the addition of a multivalent metal salt.[21,22] A variety of multivalent metal salts can lead to the same gelation effect, including Cu^{2+}, Fe^{3+}, and Ca^{2+}. A small counter anion such as Cl^{-} is used as previous work have shown that it does not lower the conductivity of PEDOT as opposed to anions such as NO_3^{-}.[23,24] Subsequently, freeze-drying followed by chemical crosslinking with 4,4′-diazido-2,2′-stilbenedisulfonic acid disodium salt (N_3-SADS) **3**[25] (Figure 1A), which was added to PEDOT solution before gelation and freeze-drying, resulted in porous structures. The chemical crosslinking was found to impart mechanical robustness to the aerogel and prevents it from disintegrating in the presence of moisture or in aqueous environment (see Supplemental Information Section 14 for details). The resulting foams are extremely lightweight due to the high air content (>97%–99.7%), and thus can be classified as aerogels (air content generally >95%). A large chunk of PEDOT aerogel can be supported by the thin awns of a wheat grass as a result of its low density (Figure 1C). These aerogels can be readily molded into virtually any shapes during the gel-formation step (Figure 1D).

PEDOT aerogels of different pore size and density can be created by controlling the PEDOT concentration (Figures S3 and S4) and the ice crystallization process prior to freeze-drying. The morphology of the hydrogel precursor was visualized using variable-pressure scanning electron microscopy (VP-SEM) and showed an interconnected fiber network (Figures 1E and S1). As the material is cooled below the freezing point of the solvent (i.e., water), ice-crystal growth causes the solids to coagulate into larger domains. Subsequent sublimation of ice crystals via lyophilization yields PEDOT foams with closed or semi-closed cell walls (Figures 1F, 1G, and S2). The pore sizes can be tuned between approximately 40 and 100 μm by controlling the freezing rate, which dictates ice-crystal sizes. The pore sizes can be further reduced by introducing an organic co-solvent, such as acetonitrile (MeCN), to suppress ice crystallization. At a 1:1 water/MeCN solvent ratio, the resulting PEDOT aerogels have pore sizes of around 5 μm and transition to an open cell structure

[1]Department of Materials Science and Engineering, Stanford University, Stanford, CA 94305, USA

[2]Department of Civil and Environmental Engineering, Stanford University, Stanford, CA 94305, USA

[3]Department of Chemical Engineering, Stanford University, Stanford, CA 94305, USA

[4]Stanford Synchrotron Radiation Lightsource, SLAC National Accelerator Laboratory, Menlo Park, CA 94025, USA

[5]Department of Bioengineering, Stanford University, Stanford, CA 94305, USA

[6]Department of Electrical Engineering, Stanford University, Stanford, CA 94305, USA

[7]Material Research Center, Samsung Advanced Institute of Technology, Yeongtong-gu, Suwon-si, Gyeonggi-do 443-803, Korea

[8]Present address: Department of Materials Science and Engineering, University of California, Merced, 5200 North Lake Road, Merced, CA 95343, USA

[9]These authors contributed equally

[10]Lead Contact

*Correspondence: zbao@stanford.edu

https://doi.org/10.1016/j.matt.2019.03.011

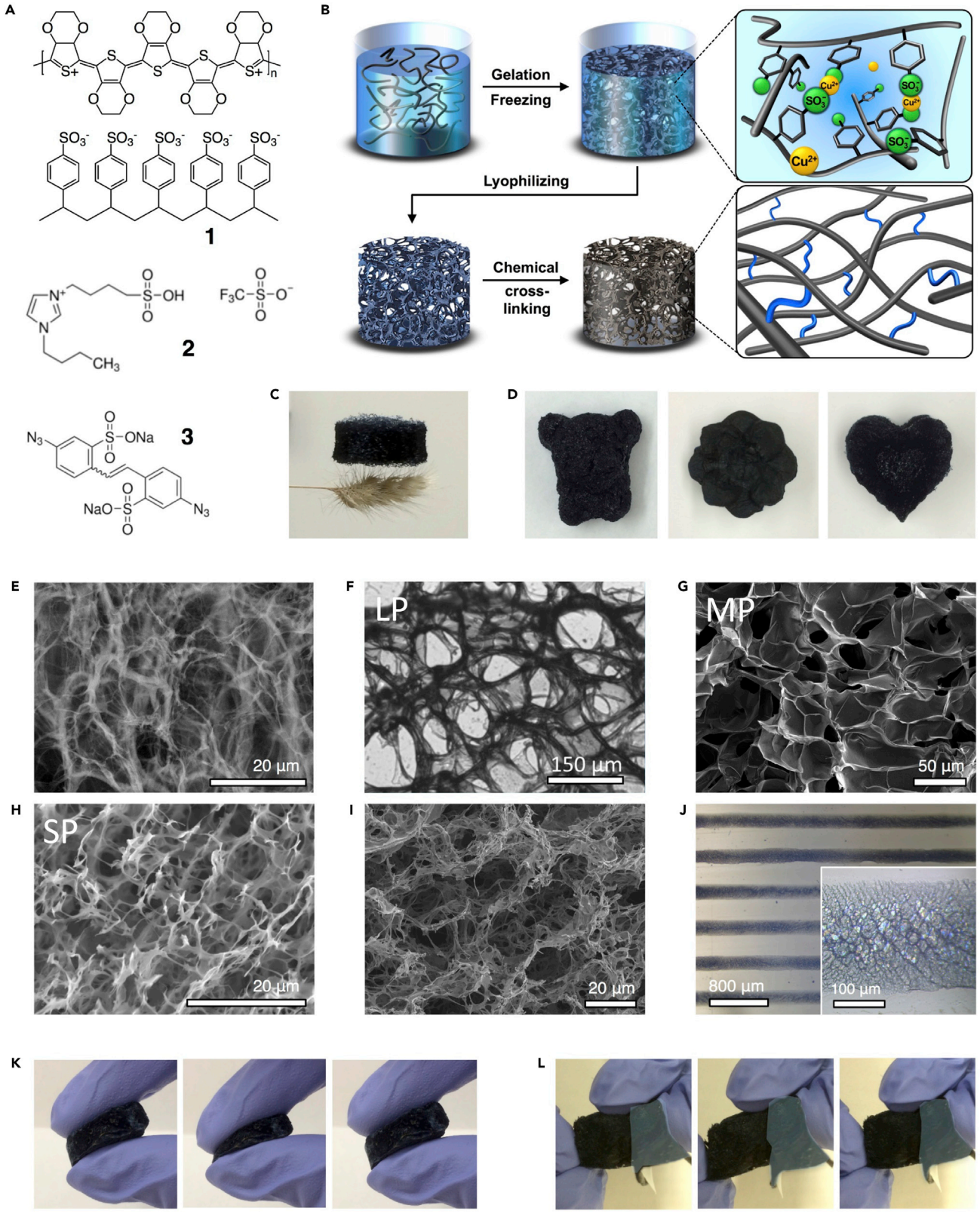
A
1
2
3
B
Gelation
Freezing
Lyophilizing
Chemical
cross-
linking
C
D
E
20 μm
F
LP
150 μm
G
MP
50 μm
H
SP
20 μm
I
20 μm
J
800 μm
100 μm
K
L

Figure 1. Overview of the Synthesis, Morphology, and Strain-Accommodating Abilities of the PEDOT Aerogels

(A) Chemical structures of PEDOT:PSS **1**, the plasticizing co-dopant 4-(3-butyl-1-imidazolio)-1-butanesulfonic acid triflate (BIBSAT) **2**, and the chemical crosslinker 4,4′-diazido-2,2′-stilbenedisulfonic acid disodium salt (N_3-SADS) **3**.

(B) Schematic of the synthetic process. Cu^{2+} is used as an example in the schematic, but other multivalent metal cations such as Fe^{3+} or Ca^{2+} lead to the same gelation effects.

(C) Photograph of a PEDOT aerogel monolith supported by the awns of a wheat grass.

(D) Photographs of PEDOT aerogels in various shapes.

(E) VP-SEM image showing the morphology of PEDOT hydrogel prior to freezing.

(F–I) Optical microscope image (F) and SEM images (G–I) of PEDOT aerogels with different pore sizes. Optical microscope image is presented for the sample in (F) instead of an SEM image due to the large pore size. (F) 5 mL PEDOT:PSS + 5 mL H_2O, freezer; (G) 5 mL PEDOT:PSS, liquid nitrogen; (H) 5 mL PEDOT:PSS + 5 mL MeCN, liquid nitrogen; (I) 5 mL PEDOT:PSS + 12 mL MeCN, liquid nitrogen.

(J) Optical microscopy image of patterned PEDOT aerogel lines on a PDMS substrate.

(K and L) Picture series showing the aerogels being reversibly compressed and stretched (see also Videos S1 and S2). The areas colored light blue are the carbon tape that served as a handle for stretching.

(Figures 1H and S2). Further increase in MeCN concentration to over 70% leads to a hierarchically porous structure with a combination of pore sizes of around 21 μm and 3 μm (Figure 1I), reminiscent of the morphology of the PEDOT hydrogel precursor shown in Figure 1E. Three representative pore sizes, denoted LP for large pore (98 ± 41 μm), MP for medium pore (52 ± 22 μm), and SP for small pore (5.3 ± 1.7 μm), which corresponds to the samples shown in Figures 1F–1H, respectively, are presented in Figure 2A and used in further exploration of their electrical and mechanical properties. Their densities are also summarized in the plot. These PEDOT aerogels are both compressible and stretchable (Figures 1K and 1L; Videos S1 and S2), rendering them uniquely suitable for potentially forming direct interfaces with the human body. The aerogel can also be readily patterned into microscopic features on an elastomeric substrate by blade-coating (Figures 1J and S5).

Conductivity of the PEDOT aerogels ranges from 0.67 to 1.84 S/cm and exhibits a dependence on pore size (Figure 2B). Notably, the densities of different aerogels are different. And a more dense aerogel contains more PEDOT for conduction. To account for this effect, all conductivity values are normalized by density. By density correction, we can obtain the intrinsic conductivity of PEDOT sheets in the aerogels (Figures 2B and S6C). SP aerogel has the highest corrected conductivity (77.4 ± 4.0 S/cm) among the three aerogels. LP and MP exhibited slightly lower corrected conductivity of 70.3 ± 29.4 S/cm and 56.1 ± 9.8 S/cm, respectively. The stretchable and compressible PEDOT aerogels described here have conductivity comparable with the previously reported PEDOT aerogels.[28–31] However, these previous ones do not exhibit any of the compressibility, stretchability, and strain- and strain-rate-invariant conductance that our aerogels possess (described in a subsequent sections). The pore-size dependence of conductivity behavior is often observed in cellular materials as the network is better interconnected in the more dense samples.[32,33] However, there is an additional variable in our system since SP aerogels were synthesized using a water/MeCN solvent mixture as opposed to purely water in LP and MP samples. Solvent environment can often have a drastic effect on the phase separation of PEDOT and PSS, which leads to different electrical properties.[34,35] X-ray photoelectron spectroscopy (XPS) analysis shows that the aerogels processed from the co-solvent system have a higher PEDOT surface content (Figure 2C), which has been attributed to enhanced conductivity in PEDOT:PSS thin films. This is likely induced by the less polar solvent environment as PEDOT is less polar than PSS. Atomic force microscopy (AFM) phase images also corroborate the higher PEDOT surface composition, which are the lighter orange areas, and show that different phase-separation morphologies arise as a result of the different solvent systems (Figure 2D). Transmission-geometry wide-angle X-ray scattering (WAXS) data reveals that the PEDOT aerogel processed from the co-solvent system

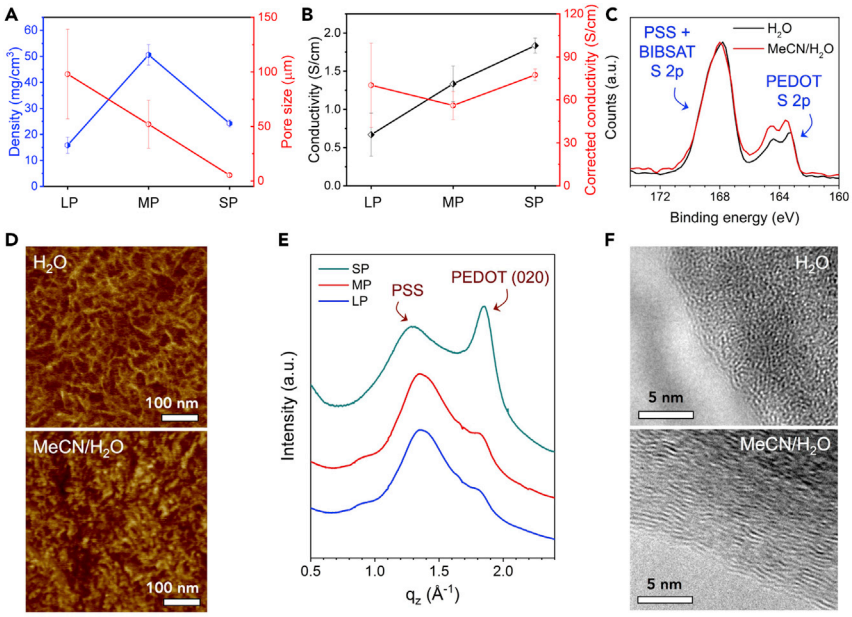

Figure 2. Chemical and Electrical Properties of the PEDOT Aerogels

(A) Density and pore size. Density was measured by dividing aerogel mass by its volume calculated from the bulk physical dimensions. Pore size was estimated by counting the pores in optical microscope and SEM images. The density of the SP samples decreased compared with MP samples because some of the ionic liquids and the PSS polymer were not completely incorporated into the final foam (see Experimental Procedures for details).

(B) Conductivity, calculated using $\sigma = l/(R * A)$, where l is the thickness, R is the resistance, and A is the cross-section area of the aerogels. Density-corrected conductivity was obtained by applying an adjustment factor based on the density difference between the aerogel and the solid material (details in Figure S6C).

(C, D, and F) XPS surface analysis profiles (C), AFM images (D), and HRTEM images (F) of PEDOT aerogels synthesized under different solvent conditions.

(E) Combined transmission-geometry WAXS near out-of-plane intensity plots of aerogels with various pore sizes obtained using different synthetic conditions. All samples share two common peaks around q_z = 1.33 Å^{-1} (d = 4.9 Å) and q_z = 1.87 Å^{-1} (d = 3.4 Å), which corresponds to the PSS amorphous scattering and PEDOT (020), respectively.[26,27] For the SP sample, the PEDOT (020) peak shifts to higher q_z while the PSS peak to lower q_z, indicating tighter π-π stacking between PEDOT chains and looser stacking between PSS. The LP and MP aerogels have an additional weak peak at ~0.89 Å^{-1} (d = ~6.8 Å), which has been observed in a previous report of PEDOT with BIBSAT plasticizer.[17]

also possesses higher crystallinity (Figures 2E and S7). This observation is further supported by high-resolution transmission electron microscopy (HRTEM) images, which illustrate more ordered interchain packing for aerogels synthesized using the water/MeCN solvent mixture (Figures 2F and S8). The combination of better connectivity, higher PEDOT surface content, and more ordered interchain packing results in the higher conductivity of aerogel from the co-solvent system.

As a result of the 3D structure and the high ductility of our PEDOT, the aerogels are both compressible and stretchable. The stiffness of the PEDOT aerogels increases with decreasing pore sizes, under both compression (Figure 3A) and tension (Figure 3D). The correlation between compressive Young's moduli and pore size is shown in Figure 3C. The Young's moduli can be tuned from ~10 kPa to >300 kPa by varying the density. Due to the exponential relationship between the density ratio versus the stiffness ratio of a solid material and the foam counterpart, the Young's moduli of the aerogel can be significantly reduced from the intrinsic value of the

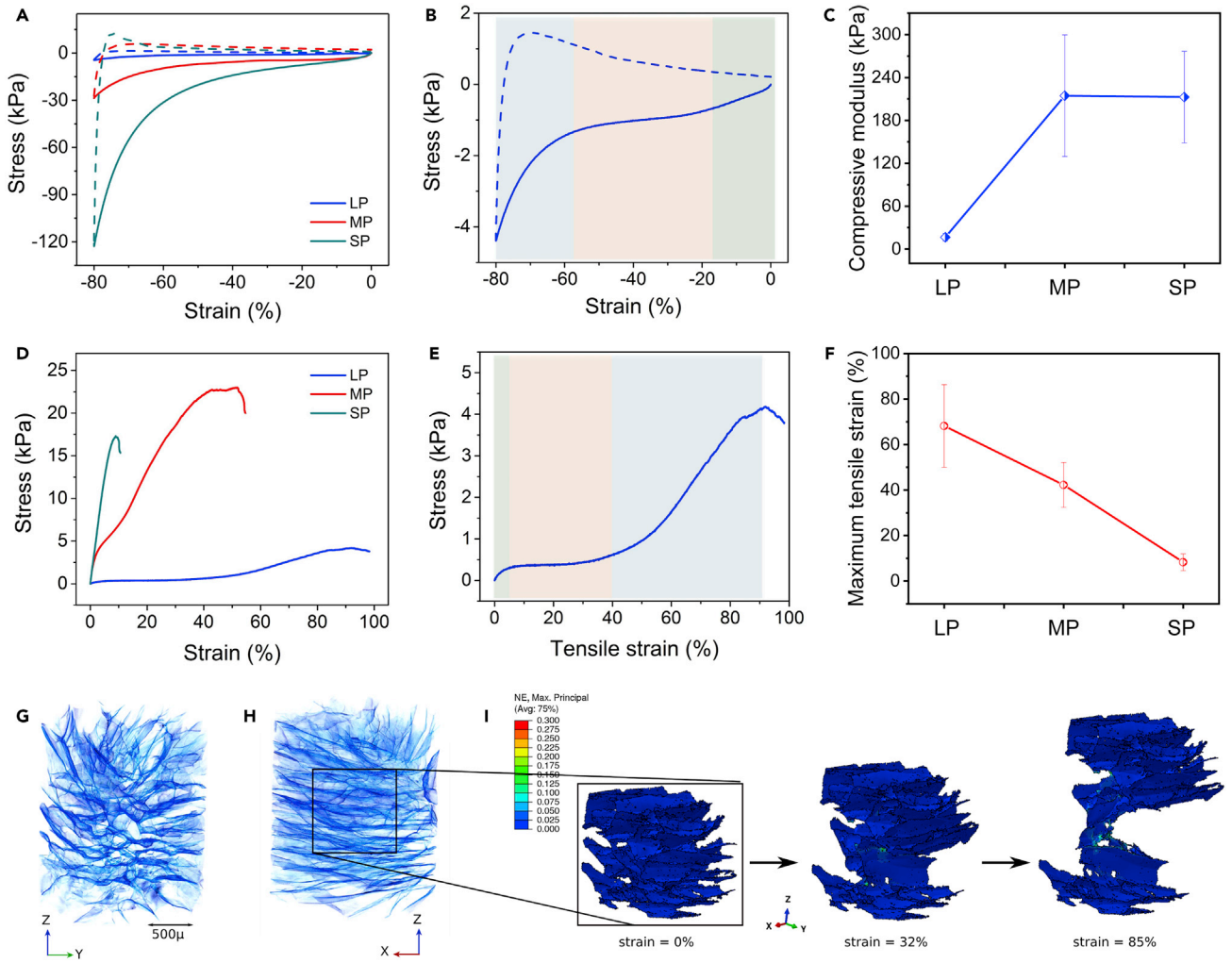

Figure 3. Mechanical Properties of PEDOT Aerogels

(A) Combined compressive stress/strain behavior of PEDOT aerogels with different pore sizes. Solid lines denote loading and dashed lines denote unloading.

(B) Compressive stress/strain behavior of LP aerogels showing the three distinctive regions of stiffness.

(C) Compressive Young's moduli.

(D) Combined tensile stress/strain behavior of PEDOT aerogels with different pore sizes.

(E) Tensile stress/strain curve of the LP aerogel showing the three distinctive regions of stiffness.

(F) Maximum tensile strain of the aerogels.

(G and H) X-ray tomography 3D reconstruction of the LP aerogel from two separate angles.

(I) Finite-element simulation modeled using the X-ray tomography reconstruction, illustrating that the 3D network deforms and starts to fracture but remains electrically connected up to the applied strain of 85%.

ductile PEDOT film (~50 MPa). The ~10- to 300-kPa stiffness of the aerogels are in the same range as various biological systems such as brain or skin, rendering this approach suitable for creating compliant human-electronic interfaces. Our PEDOT aerogel also exhibits lower Young's moduli than graphene-based aerogels of similar density, likely due to the lower stiffness of the bulk PEDOT films as compared with graphene sheets.[36,37]

A close examination of the compressive stress/strain curve revealed three distinct slopes during loading (Figures 3A and S15). As an example, the data for LP are plotted in Figure 3B. The initial linear elastic region shaded in green arises from

the rotation and bending of the struts that constitute the 3D structure at low strain. At around 20% compressive strain the material then transitions into a long, low-stiffness, elastic plateau regime (shaded in orange) where buckling within the struts becomes the predominant deformation mechanism. At around 55% compressive strain, little free volume remains between the struts and the aerogel starts to become densified, which leads to a rapid increase in stiffness (regime shaded in blue).[38] MP and SP aerogels exhibited the same behaviors with different elastic plateau ranges, [−10%, −45%] for MP and [−5%, −35%] for SP (Figure S15), where "−" denotes compression.

A tradeoff between the ultimate strength and maximum tensile strain is observed in the tensile behavior of PEDOT aerogels with different pore sizes (Figures 3D and 3F). In some applications, good ultimate strength is favorable when materials need to have good mechanical strength, for example in supercapacitors; whereas having a larger dynamic strain range and lower modulus is useful for sensing and bioelectrical measurements. Aerogels with the largest pore size have the highest maximum tensile strain of 68.2% ± 18.2%, while those with the smallest pores break at 8.3% ± 3.7% strain. The pores elongate and align along the loading direction under stretching. Larger pore sizes translate into a greater degree of free volume for deformation, thus leading to a higher maximum tensile strain (Figure 3F). On the other hand, aerogels with medium pore sizes exhibit an intermediate maximum tensile strain of 42.2% ± 9.9%, but have the highest ultimate strength of 30.1 ± 5.7 kPa.

The tensile stress/strain behavior of LP aerogel has three distinct slopes (Figure 3E). The initial linear elastic regime (shaded in green) disappears after the first two cycles, suggesting that this region could correspond to the rupturing of smaller pores at low strain, which allows them to merge into larger pores during subsequent cycles (Figure S19). The stress/strain curve then exhibits a long plateau regime (shaded in orange) that corresponds to the elongation of pores, which takes little force to deform. At around 40% tensile strain, the stiffness of the aerogel starts to increase rapidly (area shaded in blue), indicative of straining of the PEDOT struts in addition to further pore elongation. Eventually the aerogel starts to fail at ~90% strain. This high maximum tensile strain can be attributed to the collective effect of (1) the large pore sizes, (2) the chemically crosslinked and interconnected 3D network, and (3) the high ductility of our stretchable PEDOT. We found that PEDOT aerogels synthesized under identical conditions (i.e., pore sizes similar to those of the LP aerogels) but without the BIBSAT plasticizing co-dopant additives are much more brittle and have a maximum tensile strain of under 25% (Figure S9). In addition, the PEDOT aerogels without BIBSAT exhibit a much shorter plateau regime. Since the plateau regime arises from the torsion and elongation of pores, high mechanical flexibility and ductility of the strut material is crucial for its presence. Therefore, such tensile behavior is unique to our aerogel created using stretchable PEDOT.

The deformation mechanism of the microstructure was visualized by using X-ray tomography and finite-element modeling. X-ray tomography provided us with a detailed 3D image of the PEDOT aerogel (Figures 3G and 3H; Video S3), allowing us to obtain a geometrical representation of the pores and the wall/struts. We constructed a tetrahedral mesh with 950,000 nodes and 2,900,000 elements to capture the pore structures. From Figures 3G and 3H, it can be seen that the aerogel topology contains a noticeable anisotropy. Tube-like regions are visible along the plane parallel to the horizontal substrate surface. We performed a finite-element simulation on the 3D mesh and studied the material behavior under uniaxial tension. It was assumed that local response of the PEDOT walls in the aerogel is similar to

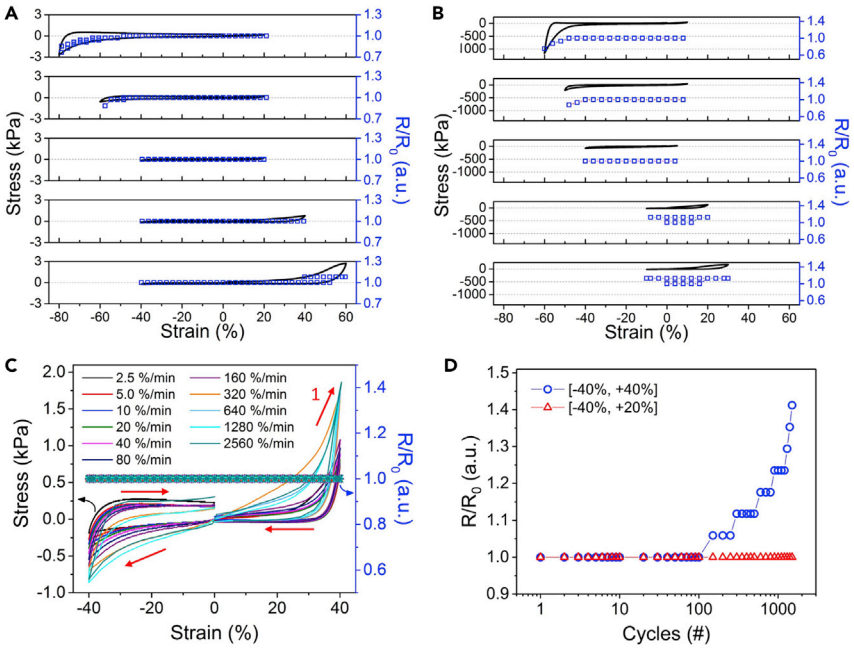

Figure 4. Strain-Electrical Properties of PEDOT Aerogels

(A and B) Correlation between different compressive and tensile strain ranges with normalized resistance values for (A) LP and (B) MP aerogels. All the strain loops have the same direction of first stretching then compression, and the individual plots are shown in Figures S16 and S17.

(C) Correlation between the stress/strain behavior and the normalized resistance obtained at various strain rates within the strain-independent range [−40%, 40%] for the LP aerogel.

(D) Cycling stability of the LP aerogel cycled between different strain ranges.

the response of a PEDOT film. Figure 3I shows the micromechanical deformation of the PEDOT aerogel during a uniaxial loading along the vertical axis (z direction). Although some sections of the aerogel are stressed starting from 32% strain in the simulation, the conductive paths did not change much in the material. The colors of Figure 3I show the maximum local engineering strain within the aerogel. This local strain is small because most of the material simply rotates or slightly bends during the mechanical loading. However, local strain became large at stress-concentration areas, initiating fractures. An in-depth explanation of the simulation methods and the role of anisotropy is discussed in detail in Supplemental Information (Section 10) and Figures S10–S12.

The normalized electrical resistance of the PEDOT aerogels with respect to strain follows closely to the stress/strain behavior, and a strain-invariant resistance (SIR) range can be identified for each aerogel with different pore sizes (Figures 4A, 4B, S16, and S17). We strained the LP aerogels through various strain intervals, and found that they have an SIR range of [−40%, +40%], where "−" denotes compression and "+" tension. This interval corresponds well with the plateau regimes of the compressive and tensile stress/strain curves where mechanical deformation is mostly limited to bending, torsion, and flexing of the 3D network, which has very limited effect on the electrical properties of a highly flexible and ductile material. Resistance of the aerogel network decreases as the 3D network enters the densification regime (i.e., beyond −40% strain) where the struts come into close contact with each other, forming a better percolated network. When the aerogel is elongated beyond the tensile plateau regime, the PEDOT struts start to experience tension and then fracture, which leads to an increase in aerogel resistance. Such an observation agrees with

the finite-element simulation result that suggests the stress falls on the PEDOT struts rather than the 3D structure beyond 32% tensile strain. This resistance increase is possibly caused by strut elongation and reduced number of conduction pathways induced by struts breaking under tension. The resistance of our LP aerogel remains unchanged at 40% strain, and R/R_0 is only 1.1 at 60% strain (Figure 4A). In comparison, a cracked gold thin film stretchable electrode on polydimethylsiloxane (PDMS) substrate exhibited an R/R_0 value of 10 at 50% strain.[39] Our previously reported stretchable PEDOT:PSS film had an R/R_0 value of 0.36 at 50% strain and 2.16 at 150% strain.[17]

Furthermore, the LP PEDOT aerogel can retain electrical contact until over 570% tensile strain (Figure S14). Due to the multi-junction nature of the 3D structures, breakage of individual junctions does not directly initiate crack propagation in other struts. Hence, the aerogel fractures at a slow rate and remains conductive (albeit an >75-fold increase in resistance) even when there are just a few fibers dangling at around 570% strain.

The SIR range is dictated by the pore sizes of the aerogels. The MP PEDOT aerogel exhibits an SIR interval of [−40%, +10%] strain. The lower tensile strain boundary condition compared with the LP samples is a result of the more limited degree of freedom for structural deformation. This effect arises from the smaller pore sizes and more continuous PEDOT struts (Figure 1G).

In addition, the PEDOT aerogels exhibit a large strain-rate-invariant resistance (SRIR) from 2.5%/min to 2,560%/min when cycled within the SIR range, regardless of pore sizes (Figures 4C and S18). Since compression and tension only result in bending, flexing, and torsion of the PEDOT struts, strain rate has little influence over the bulk electrical properties of the 3D network and is independent of the viscoelastic properties of the materials of which it is composed. The strain-rate dependence of the stress-strain relationship is an indication of presence of pore structures that respond to strain at different time scales. For example, at lower strain rates some of the thin sheets may rotate and unbend so that less local strain is applied on the sheets while at higher strain rates they may simply be stretched. On the other hand, conductance of the aerogel is more sensitive to strain itself instead of strain rate, since conductivity is more related to the number of conducting pathways present and the conductivity and connectivity of the pathways. Therefore, the strain rate may not affect conductance as long as the conduction pathways are not affected by strain rate. Even if there may be difference in the local strain of the thin sheets at different strain rates, the conductivity can still remain the same because the number of conducting pathways remains unchanged and the conductivity and connectivity of these pathways are not very different. It is possible that there might be small fluctuation in conductance due to different strain rate, which was beyond our detection limit. In our work, we found that pore size did not really affect the strain-rate-related behavior, because stress is always sensitive to strain rate while conductivity is not affected as much as long as we are cycling the aerogels in the SIR range. The presence of the SIR and SRIR intervals both for tension and compression is unique to this 3D structuring approach. Such properties are attractive for potential application in wearable and epidermal electronics, as the human body is dynamic with different degrees of motion at various speeds. The close correlation between the stress/strain behavior and resistance change also serves as a powerful route for identifying and predicting the presence and range of SIR and SRIR in a given 3D structure simply through mechanical testing.

Furthermore, the aerogels show remarkable stability under repeated cycling (Figures 4D and S19–S22). When the LP samples were cycled within the full SIR range of [−40%, +40%] strain at 160%/min, the resistance remains constant until approximately 100 cycles. It then increases consistently, likely due to strut breakage at various junctions since 40% strain is close to the inflection point in the stress/strain curve where struts start to become stressed. However, if the tension boundary is reduced to [−40%, +20%] strain, which is well within the tensile plateau regime, the resistance of the aerogel remains constant even after 1,400 cycles, demonstrating excellent damage tolerance for potential repeated and reversible usage in electronic devices.

Owing to the chemically crosslinked nature of the PEDOT aerogels, they retain good mechanical robustness even in moist or aqueous environments. The struts of the uncrosslinked PEDOT aerogels swell significantly in water, thus rendering the hydrated aerogels easy to rupture (Figures S23A and S23B; Video S4). Chemical crosslinking limits the degree of swelling and leads to high robustness in water that allows the aerogel to be compressed to a fraction of its original volume elastically (Figures S23C and S23D; Video S5). The resistance of the aerogel increases by about 4-fold after soaking in water, but stabilizes after about 30 min with a final resistance plateau well below 10 Ω (Figure S23E). The unique combination of high aqueous mechanical and electrical stability suggests potential applications in biological applications such as tissue engineering and implantable electronics. As a proof of concept, an aerogel film is used as a dry electrode for electrocardiogram (ECG) measurements. Commercial ECG electrodes utilize an ionically conductive gel at the electrode-skin interface that dries out over time and can irritate the skin. Efforts invested in dry gold electrodes solve the skin irritation issue, but in comparison fade in signal detection due its sensitivity to movement. In contrast, the electrically conductive aerogel films are dry and breathable due to the high porosity. The ECG signals from the aerogel electrodes lead to clearly visible, characteristic R and T peaks (Figure S24C), whereas only the characteristic R peak is distinct in the dry gold electrode control (Figure S24D). While the conductive material density of the aerogel at the skin interface is lower than that of gold, the enhanced performance can be attributed to superior flexibility of the soft aerogel, demonstrating its potential for human-machine interfaces.

Conclusions

In contrast to previous efforts such as nanocomposites or intrinsically stretchable conductors, we demonstrated a 3D structuring approach for a conducting polymer that can lead to electrical resistance that is independent of strain and strain rate over a broad range, under both compression and tension, and exhibits remarkable cycling stability. Such unique properties are imparted by controlling the porosity and the highly ductile nature of our PEDOT:PSS material. In addition, these aerogels are ultra-lightweight, patternable, compliant, and mechanically and electrically robust in both solid-state and aqueous environments. This synergistic combination of properties renders this an attractive new approach for creating strain-accommodating conductors and electronics.

EXPERIMENTAL PROCEDURES

Synthesis of PEDOT Aerogels

In a typical synthesis, 45.5 wt % of the BIBSAT plasticizing co-dopant **2** (Santa Cruz Biotechnology), 5 wt % of the N_3-SADS crosslinker **3** (Sigma-Aldrich), and 3 mol % of a metal salt with a multivalent cation (e.g., $CuCl_2$) (Sigma-Aldrich) that acts as a gelation agent were mixed into the Agfa ICP1050 PEDOT:PSS **1** dispersion, in the order stated, under rapid stirring. The percentages of additive were calculated with respect to the

PEDOT:PSS solid content. The mixture was either directly frozen in a freezer at −18°C or placed in an oven for 4 h to induce gelation prior to freezing using liquid nitrogen. The excess liquid surrounding the gel was removed before freezing. In the case of SP aerogels, some ionic liquid and potentially PSS polymer were partially removed if they were dissolved in the removed liquid. The detailed variation in solvent, gelation, and freezing conditions applied to achieve different pore sizes are summarized in Table S1. The frozen solvent was then sublimed by freeze-drying at −85°C on an SP Scientific VirTis lyophilizer, leaving voids of similar sizes and geometries as pores. Finally, the porous network was chemically crosslinked by the bisazide compound **3** in a vacuum oven purged three times with nitrogen at 180°C to enhance its robustness.

Patterning of PEDOT Aerogels

To show the general applicability of the PEDOT aerogel in electronic devices, we demonstrated its patterning with a feature size below 200 μm on a PDMS substrate. Narrow lines of the materials were achieved by blade-coating a viscous dispersion of the PEDOT:PSS (formulation details in Table S1) through a stencil mask. Prior to deposition, a short oxygen plasma surface treatment (10 s at 150 W) was carried out through the mask to improve the wettability of the substrate on the exposed areas. The plasma treatment also helped to improve the definition of the lines by avoiding overflowing of the material beyond the exposed areas when the stencil mask was removed. The stencil mask was fabricated by mechanically cutting the desired pattern on a transparency sheet 100 μm thick using a computer numerical control cutter (Silhouette Cameo). The whole printing process took place on a substrate cooled at around −18°C to delay water evaporation from the hydrogel. Immediately after patterning, the substrate with the wet patterned lines was introduced into a small closed container and stored inside a freezer. Once frozen, the patterned lines were subjected to the freeze-drying process similarly to the bulk samples that provided their porous structure.

Electrical Property Measurements

The resistance of the aerogel was tested by sandwiching an aerogel between two pieces of copper films using silver paste as the adhesive (for more details see Supplemental Information Section 6). The volume of air was taken into consideration in the conductivity calculation by applying an adjustment factor based on the density difference between the aerogel and the solid material (Figure S6C).[29]

Mechanical Property Testing

The stress/strain and cycling behavior of the aerogel and their correlation to the electrical properties were tested using an Instron 5565 with a 100-N loading cell. The samples were glued between compression plates using the configuration depicted in Figure S13. A strain rate of 20%/min was used for mechanical testing if not otherwise indicated. LP aerogels have rectangular symmetry with sample size of 30 × 30 × 6 mm (width × length × height). MP and SP aerogels have circular symmetry with sample size (diameter × height) of 19.5 × 7.6 mm and 16.5 × 10.5 mm, respectively. Small deviations exist in sample size for different aerogel samples. The loading and unloading directions were marked on the plots and shown in the schematic in Figure S13.

Chemical and Morphological Characterization

XPS was performed on a PHI VersaProbe Scanning X-ray Photoelectron Spectroscopy Microprobe. A Leica DM4000 M LED microscope was used for optical microscope images. SEM images were collected on an FEI XL30 Sirion scanning electron microscope with 5 kV accelerating voltage. Pore sizes of different aerogels were

estimated from optical microscope and SEM images by counting the pores. TEM images were collected on an FEI Tecnai TF20 transmission electron microscope operating at 200 kV. AFM images were acquired using a Veeco Multimode atomic force microscope in tapping mode.

Transmission-Geometry Wide-Angle X-Ray Scattering

WAXS patterns were collected using two different synchrotron X-ray beamlines: beamline 11-3 at the Stanford Synchrotron Radiation Lightsource of SLAC National Accelerator Laboratory (SLAC), with a photon energy of 12.735 keV and sample-to-detector distance of 320 mm; and beamline 7.3.3 at the Advanced Light Source of Lawrence Berkeley National Laboratory, with a photon energy of 10 keV at a sample-to-detector distance of 309 mm.[40] In both setups, freestanding films of aerogels were used in a transmission geometry. The 2D X-ray scattering data images are reduced into scattering curve profiles using NIKA package for Igor Pro software.[41]

X-Ray Tomography

Computed tomography (CT) scans of the 3D structured aerogel were collected using the Zeiss Xradia 520 Versa X-ray microscope. A total of 2,501 CT scans were taken at 30 kV for 360° and reconstructed to create a 3D rendering of the interior morphology of the samples.

Finite-Element Simulation

We used the Computational Geometry Algorithms Library[42] to obtain the surfaces of the aerogel and create a triangular surface mesh from the X-ray tomography data. We then incorporated the iso2mesh MATLAB library[43] to create a volumetric mesh. The mesh contains 937,673 nodes and 2,962,452 tehrahedral elements. We used the compressible Neo-Hookean hyperelastic model with Young modulus of 100 MPa and the Poisson ratio of 0.45, closely resembling the mechanical tests of PEDOT in bulk form. Additionally, a damage criterion is specified that limits the local strain of PEDOT below 40%. When the material locally reaches this strain, damage occurs in the material and results in the reduction of the stress-carrying capacity of PEDOT and ultimately the complete removal of some elements in the localized high-stress regions. The specimen is stretched along the z axis while all nodes are free to move in both x and y directions. All nodes located at the bottom 10% of the specimen are fixed in z direction and the nodes at the top 10% of the specimen are pulled in the positive z direction by 40% of the total length of the specimen. We ran the simulation using ABAQUS Standard version 6.12 with quasi-static loading conditions. The maximum principal strain is plotted in Figure S11.

Characterization as ECG Electrode

Prior to the work described in this manuscript, an IRB review waiver was obtained from the Stanford IRB Office. The project does not involve human subjects as defined by federal guidelines. The work is not about living individuals and does not include collection of individually identifiable private information.

SUPPLEMENTAL INFORMATION

Supplemental Information can be found online at https://doi.org/10.1016/j.matt.2019.03.011.

ACKNOWLEDGMENTS

We gratefully acknowledge Justin Sao for assistance with sample preparation, Allison Hinckley and Prof. Wei Cai for stimulating discussions, and Prof. Chaitan Khosla and Peter Kim for access to their lyophilizer. We thank Agfa for providing

PEDOT:PSS ICP1050. This work was sponsored by Samsung Electronics, H.Y. thanks support from SLAC National Accelerator Laboratory. Part of the X-ray scattering measurements were performed at beamline 11-3 of the Stanford Synchrotron Radiation Lightsource (SSRL), SLAC National Accelerator Laboratory, which is supported by the US Department of Energy, Office of Science, Office of Basic Energy Sciences under contract no. DE-AC02-76SF00515. Part of the X-ray scattering measurements were performed at beamline 7.3.3 at Advanced Light Source (ALS), Lawrence Berkeley National Laboratory, which is supported by the Director of the Office of Science, Office of Basic Energy Sciences of the US Department of Energy under contract no. DE-AC02-05CH11231. We thank the beamline scientists Tim Dunn (SSRL) and Chenhui Zhu (ALS) for the user support at the beamlines. Y.L. is supported by a National Science Scholarship (A*STAR, Singapore). F.M.-L. was partly supported by the Swiss National Science Foundation under the Early Mobility Postdoc Project no. P2ELP2_155355 and the Department of Energy Basic Science (USA) grant no. DE-SC0016523. K.C. thanks support from the Stanford ChEM-H Chemistry/Biology Interface Predoctoral Training Program and the National Institute of General Medical Sciences of the National Institutes of Health under award number T32GM120007. C.L. acknowledges support from the National Science Foundation through CMMI-1553638.

AUTHOR CONTRIBUTIONS

Conceptualization, Y.W. and Z.B.; Structural Investigation, G.C., Y.W., H.Y., Y.J., S.C., F.M.-L., L.J., K.C., and J.W.C.; Device Fabrication and Evaluation, G.C., Y.W., V.F., Y.L. F.L., and E.P.; Simulation, R.R. and C.L.; Writing, G.C., R.R., Y.W., and Z.B.; Supervision, Z.B. All authors discussed the results and commented on the manuscript at all stages.

DECLARATION OF INTERESTS

The authors declare no competing interests.

Received: December 18, 2018
Revised: February 24, 2019
Accepted: March 18, 2019
Published: April 18, 2019

REFERENCES

1. Wang, S., Oh, J.Y., Xu, J., Tran, H., and Bao, Z. (2018). Skin-inspired electronics: an emerging paradigm. Acc. Chem. Res. *51*, 1033–1045.

2. Rogers, J., Malliaras, G., and Someya, T. (2018). Biomedical devices go wild. Sci. Adv. *4*, eaav1889.

3. Someya, T., Bao, Z., and Malliaras, G.G. (2016). The rise of plastic bioelectronics. Nature *540*, 379.

4. Hammock, M.L., Chortos, A., Tee, B.C.K., Tok, J.B.H., and Bao, Z. (2013). 25th anniversary article: the evolution of electronic skin (e-skin): a brief history, design considerations, and recent progress. Adv. Mater. *25*, 5997–6038.

5. Wagner, S., and Bauer, S. (2012). Materials for stretchable electronics. MRS Bull. *37*, 207–213.

6. Kim, D.-H., and Rogers, J.A. (2008). Stretchable electronics: materials strategies and devices. Adv. Mater. *20*, 4887–4892.

7. Wang, J., Lin, M.-F., Park, S., and Lee, P.S. (2018). Deformable conductors for human–machine interface. Mater. Today *21*, 508–526.

8. Fu, H., Xu, S., Xu, R., Jiang, J., Zhang, Y., Rogers, J.A., and Huang, Y. (2015). Lateral buckling and mechanical stretchability of fractal interconnects partially bonded onto an elastomeric substrate. Appl. Phys. Lett. *106*, 091902.

9. Kim, D.-H., Ahn, J.-H., Choi, W.M., Kim, H.-S., Kim, T.-H., Song, J., Huang, Y.Y., Liu, Z., Lu, C., and Rogers, J.A. (2008). Stretchable and foldable silicon integrated circuits. Science *320*, 507–511.

10. Shyu, T.C., Damasceno, P.F., Dodd, P.M., Lamoureux, A., Xu, L., Shlian, M., Shtein, M., Glotzer, S.C., and Kotov, N.A. (2015). A Kirigami approach to engineering elasticity in nanocomposites through patterned defects. Nat. Mater. *14*, 785–789.

11. Blees, M.K., Barnard, A.W., Rose, P.A., Roberts, S.P., McGill, K.L., Huang, P.Y., Ruyack, A.R., Kevek, J.W., Kobrin, B., Muller, D.A., et al. (2015). Graphene Kirigami. Nature *524*, 204–207.

12. Kim, Y., Zhu, J., Yeom, B., Di Prima, M., Su, X., Kim, J.-G., Yoo, S.J., Uher, C., and Kotov, N.A. (2013). Stretchable nanoparticle conductors with self-organized conductive pathways. Nature *500*, 59–63.

13. Sekitani, T., Noguchi, Y., Hata, K., Fukushima, T., Aida, T., and Someya, T. (2008). A rubberlike stretchable active matrix using elastic conductors. Science *321*, 1468–1472.

14. Son, D., and Bao, Z. (2018). Nanomaterials in skin-inspired electronics: toward soft and robust skin-like electronic nanosystems. ACS Nano. https://doi.org/10.1021/acsnano.8b07738.

15. Matsuhisa, N., Inoue, D., Zalar, P., Jin, H., Matsuba, Y., Itoh, A., Yokota, T., Hashizume, D., and Someya, T. (2017). Printable elastic conductors by in situ formation of silver nanoparticles from silver flakes. Nat. Mater. *16*, 834.

16. Choi, S., Han, S.I., Jung, D., Hwang, H.J., Lim, C., Bae, S., Park, O.K., Tschabrunn, C.M., Lee, M., Bae, S.Y., et al. (2018). Highly conductive, stretchable and biocompatible Ag-Au core-sheath nanowire composite for wearable and implantable bioelectronics. Nat. Nanotechnol. *13*, 1048–1056.

17. Wang, Y., Zhu, C., Pfattner, R., Yan, H., Jin, L., Chen, S., Molina-Lopez, F., Lissel, F., Liu, J., Rabiah, N.I., et al. (2017). A highly stretchable, transparent, and conductive polymer. Sci. Adv. *3*, e1602076.

18. Oh, J.Y., Kim, S., Baik, H.-K., and Jeong, U. (2015). Conducting polymer dough for deformable electronics. Adv. Mater. 4455–4461.

19. Lipomi, D.J., Lee, J.A., Vosgueritchian, M., Tee, B.C.K., Bolander, J.A., and Bao, Z. (2012). Electronic properties of transparent conductive films of PEDOT: PSS on stretchable substrates. Chem. Mater. *24*, 373–382.

20. Savagatrup, S., Chan, E., Renteria-Garcia, S.M., Printz, A.D., Zaretski, A.V., O'Connor, T.F., Rodriquez, D., Valle, E., and Lipomi, D.J. (2015). Plasticization of PEDOT: PSS by common additives for mechanically robust organic solar cells and wearable sensors. Adv. Funct. Mater. *25*, 427–436.

21. Zhang, X., Chang, D., Liu, J., and Luo, Y. (2010). Conducting polymer aerogels from supercritical CO_2 drying PEDOT-PSS hydrogels. J. Mater. Chem. *20*, 5080–5085.

22. Sandu, G., Ernould, B., Rolland, J., Cheminet, N., Brassinne, J., Das, P.R., Filinchuk, Y., Cheng, L., Komsiyska, L., Dubois, P., et al. (2017). Mechanochemical synthesis of PEDOT: PSS hydrogels for aqueous formulation of Li-ion battery electrodes. ACS Appl. Mater. Interfaces *9*, 34865–34874.

23. Xia, Y., and Ouyang, J. (2009). Salt-induced charge screening and significant conductivity enhancement of conducting poly(3,4-ethylenedioxythiophene):poly(styrenesulfonate). Macromolecules *42*, 4141–4147.

24. Ouyang, J. (2013). "Secondary doping" methods to significantly enhance the conductivity of PEDOT: PSS for its application as transparent electrode of optoelectronic devices. Displays *34*, 423–436.

25. Brase, S., Gil, C., Knepper, K., and Zimmermann, V. (2005). Organic azides: an exploding diversity of a unique class of compounds. Angew. Chem. *44*, 5188–5240.

26. Palumbiny, C.M., Liu, F., Russell, T.P., Hexemer, A., Wang, C., and Müller-Buschbaum, P. (2015). The crystallization of PEDOT: PSS polymeric electrodes probed in situ during printing. Adv. Mater. *27*, 3391–3397.

27. Aasmundtveit, K.E., Samuelsen, E.J., Pettersson, L.A.A., Inganas, O., Johansson, T., and Feidenhans, R. (1999). Structure of thin films of poly(3,4-ethylenedioxythiophene). Synth. Met. *101*, 561–564.

28. Guex, A.G., Puetzer, J.L., Armgarth, A., Littmann, E., Stavrinidou, E., Giannelis, E.P., Malliaras, G.G., and Stevens, M.M. (2017). Highly porous scaffolds of PEDOT: PSS for bone tissue engineering. Acta Biomater. *62*, 91–101.

29. Gordon, M.P., Zaia, E.W., Zhou, P., Russ, B., Coates, N.E., Sahu, A., and Urban, J.J. (2017). Soft PEDOT: PSS aerogel architectures for thermoelectric applications. J. Appl. Polym. Sci. *134*, 44070.

30. Zhang, X., Li, C., and Luo, Y. (2011). Aligned/unaligned conducting polymer cryogels with three-dimensional macroporous architectures from ice-segregation-induced self-assembly of PEDOT-PSS. Langmuir *27*, 1915–1923.

31. Khan, Z.U., Edberg, J., Hamedi, M.M., Gabrielsson, R., Granberg, H., Wågberg, L., Engquist, I., Berggren, M., and Crispin, X. (2016). Thermoelectric polymers and their elastic aerogels. Adv. Mater. *28*, 4556–4562.

32. Lee, J.H., Singer, J.P., and Thomas, E.L. (2012). Micro-/nanostructured mechanical metamaterials. Adv. Mater. *24*, 4782–4810.

33. Scocchi, G., Ortona, A., Grossi, L., Bianchi, G., D'Angelo, C., Leidi, T., and Gilardi, R. (2013). Evaluation of a simple finite element method for the calculation of effective electrical conductivity of compression moulded polymer-graphite composites. Compos. Part A Appl. Sci. Manuf. *48*, 15–25.

34. Xia, Y.J., and Ouyang, J.Y. (2011). PEDOT:PSS films with significantly enhanced conductivities induced by preferential solvation with cosolvents and their application in polymer photovoltaic cells. J. Mater. Chem. *21*, 4927–4936.

35. Kim, Y.H., Sachse, C., Machala, M.L., May, C., Muller-Meskamp, L., and Leo, K. (2011). Highly conductive PEDOT:PSS electrode with optimized solvent and thermal post-treatment for ITO-free organic solar cells. Adv. Funct. Mater. *21*, 1076–1081.

36. Zhang, B.X., Zhang, J.L., Sang, X.X., Liu, C.C., Luo, T., Peng, L., Han, B.X., Tan, X.N., Ma, X., Wang, D., et al. (2016). Cellular graphene aerogel combines ultralow weight and high mechanical strength: a highly efficient reactor for catalytic hydrogenation. Sci. Rep. *6*, 25830.

37. Wu, Y.P., Yi, N.B., Huang, L., Zhang, T.F., Fang, S.L., Chang, H.C., Li, N., Oh, J., Lee, J.A., Kozlov, M., et al. (2015). Three-dimensionally bonded spongy graphene material with super compressive elasticity and near-zero Poisson's ratio. Nat. Commun. *6*, 6141.

38. Gladysz, G.M., and Chawla, K.K. (2015). Voids in Materials: From Unavoidable Defects to Designed Cellular Materials (Elsevier), pp. 1–201.

39. Zhang, B., Lei, J., Qi, D., Liu, Z., Wang, Y., Xiao, G., Wu, J., Zhang, W., Huo, F., and Chen, X. (2018). Stretchable conductive fibers based on a cracking control strategy for wearable electronics. Adv. Funct. Mater. *28*, 1801683.

40. Hexemer, A., Bras, W., Glossinger, J., Schaible, E., Gann, E., Kirian, R., MacDowell, A., Church, M., Rude, B., and Padmore, H. (2010). A SAXS/WAXS/GISAXS beamline with multilayer monochromator. J. Phys. Conf. Ser. *247*, 012007.

41. Ilavsky, J. (2012). Nika: software for two-dimensional data reduction. J. Appl. Crystallogr. *45*, 324–328.

42. Rineau, L., and Yvinec, M. (2017). CGAL 4.10: 3D Surface Mesh Generation. https://doc.cgal.org/4.10/Surface_mesher/index.html.

43. Fang, Q.Q., and Boas, D.A. (2009). Tetrahedral mesh generation from volumetric binary and gray-scale images. 2009 IEEE International Symposium on Biomedical Imaging: From Nano to Macro, Vols. 1 and 2, 1142–1145.